

Bloch beamsplitters and dual-lattice methods for atom interferometry

Zachary Pagel,^{*} Weicheng Zhong, Richard H. Parker, Christopher T. Olund, Norman Y. Yao, and Holger Müller[†]
Department of Physics, University of California Berkeley, Berkeley, CA 94720
 (Dated: May 26, 2022)

Using two independently accelerated optical lattices, we produce a coherent beamsplitter for atom interferometry, as well as coherent reflection and recombination of matter waves when the lattices are ramped through velocity degeneracy. These methods enable large momentum transfer interferometers with applications in precision measurement, inertial sensing, and searches for new physics. The dual-lattice dynamics are shown to be adiabatic, similar to Bloch oscillations in a single lattice, and loss mechanisms and systematic effects are discussed. The techniques are implemented experimentally and shown to be phase-stable using a differential measurement between two Mach-Zehnder (MZ) atom interferometers. In a single MZ-interferometer, contrast is observed at up to $240\hbar k$ momentum splitting, one of the largest coherent momentum splittings achieved to date.

I. INTRODUCTION

Light-pulse atom interferometry uses photons to coherently manipulate atomic wavefunctions for, e.g., precision measurements of the fine structure constant [1, 2], Newton’s gravitational constant [3, 4], tests of the weak equivalence principle [5, 6] and dark energy theories [7, 8], as well as precision gravimetry [9, 10] and gradiometry [11]. Large momentum transfer (LMT) has allowed us to separate atomic wave packets with the momentum of $n = 100$ ’s of photons [1, 12, 13]. LMT is often based on multi-photon Bragg diffraction [14, 15]. This method, however, is relatively inefficient as small laser intensity variations strongly affect the efficiency, requires large laser intensity (proportional to n^2 or even n^4 , if scattering losses are to be kept constant) and causes systematic errors known as diffraction phases [16–18]. Bloch oscillations of atoms in an optical lattice enable $n = 100$ ’s of photons to be transferred with a laser intensity that is nearly independent of n [19, 20]. It was shown theoretically that two accelerated optical lattices could be used as a beam splitter [21], but experimentally this has not been realized; Bloch-Bragg combinations with Bloch oscillations in two lattices have been used, where the wave packets are initially separated using Bragg diffraction [1, 13, 22, 23]. Likewise, accelerated lattices have not been shown to symmetrically reflect a pair of wave packets towards each other, as required for proposed dark-matter and gravitational-wave detectors [24].

Here, we extend the toolbox of coherent atom manipulation by demonstrating beamsplitters and mirrors with two superposed optical lattices that are accelerated through velocity degeneracy. These methods use lower laser power than Bloch-Bragg combinations [22, 23], have zero diffraction phase by symmetry, and approach 100% efficiency (see Figure 1). We demonstrate state-of-the-art LMT with $240\hbar k$ as well as interferometry with nearly fully-guided matter waves. These methods will enable next-generation atom interferometry measurements

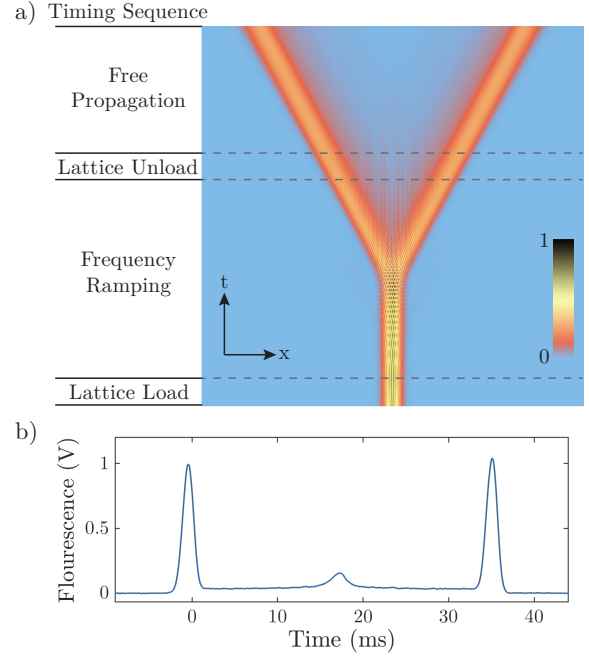


FIG. 1. a) Density plot of $|\psi(x, t)|$ from numerical simulation of a Bloch beamsplitter with a lattice depth $U_0 = 1.3 E_r$ and ramp rate $r = 0.2 \omega_r^2$. Timing sequence is indicated on the left. The initial wavefunction is a Heisenberg limited gaussian wavepacket with velocity spread $0.05 v_r$ corresponding to our experimental temperature. Frequencies are ramped for one Bloch period, corresponding to $4\hbar k$ slitting between arms. b) Experimental time of flight fluorescence trace showing an efficient $60\hbar k$ beamsplitter with a ramp rate $r = 0.26 \omega_r^2$, and a lattice depth around $1.5 E_r$.

of the fine-structure constant, searches for gravitational waves, or searches for new physics [6, 8, 24–26].

The Bloch beamsplitter described here begins with a pair of optical lattices that are superposed such that they add constructively to form a single lattice. Atoms below the recoil temperature are loaded into the ground state of this lattice. By ramping optical frequencies, the lattices are accelerated away from one another and the atomic wave function is adiabatically and coherently split

^{*} zpagel@berkeley.edu

[†] hm@berkeley.edu

between the two lattices. In the context of atom-beam experiments, it was numerically demonstrated that this Hamiltonian can produce an efficient beamsplitter, although the idea was never extended to conventional atom interferometers [21]. Crucially, in analogy with Bloch oscillations in a single lattice, we find that the permissible velocity class of atoms that can undergo efficient dynamics is independent of the momentum splitting. We also show that the relative phase of the optical lattices when accelerating lattice through velocity degeneracy, we can realize symmetric reflection or recombination of atomic wave-packet trajectories.

The dynamics of the process are studied using the symmetry of the Hamiltonian under momentum inversion. We simultaneously diagonalize the Hamiltonian in momentum-parity and energy, and a Bloch beamsplitter can be understood as an atom adiabatically following the even-parity ground state of the Hamiltonian. This parity basis is then used to study effects such as non-adiabatic losses, dynamics while ramping the lattices through velocity degeneracy, and systematic effects from experimental imperfections.

Together, these lattice operations allow for one to construct LMT interferometers only using accelerated lattices. We demonstrate a Mach-Zehnder (MZ) interferometer with momentum splittings up to $240\hbar k$, compared to $102\hbar k$ that have been achieved with a succession of $2\hbar k$ Bragg pulses [12], or $408\hbar k$ by combining Bragg diffraction with Bloch oscillations [13, 22]. A differential measurement between two simultaneous MZ interferometers shows a stable phase between the interferometer outputs, demonstrating that the methods are first-order coherent and phase-stable.

II. THEORY

To understand the lattice beamsplitter, we will first derive a unitary transformation for the dual-lattice Hamiltonian that isolates the relevant dynamics (Sect. II A). Near velocity degeneracy, it was previously expected that near-resonant effects from the second lattice would cause too large of a perturbation to the dynamics of atoms in the first lattice to permit an efficient beamsplitter. We show that the effects of the perturbation terms can remain small within the rotating wave approximation under certain conditions, resulting in an adiabatic process (Sect. II B). The simplified dual-lattice Bloch oscillation (DLBO) Hamiltonian is nearly identical to the standard single-lattice Bloch oscillation (SLBO) Hamiltonian, differing only in being invariant under momentum inversion. As a result, the DLBO eigenstates are symmetric and anti-symmetric in momentum space.

We then study loss mechanisms that reduce the amplitude of the ground state; we find that they include standard Landau-Zener tunneling due to energy-level crossings as well as higher-order transitions which are possible due to perturbation terms dropped in the rotating wave

approximation. (Sect. II C). The condition for validity of the rotating wave approximation, Landau-Zener losses and higher-order losses all give non-linear conditions on the permissible lattice accelerations, and in total they allow for the dual-lattice processes to approach 100% efficiency in the limit of slowly accelerated lattices (Sect. II D). The dynamics are also discussed for lattices that are ramped through velocity degeneracy, showing that an offset laser phase can be used to coherently control the output population in the two lattices (Sect. II E). Last, we discuss some important experimental requirements in order to realize these methods in the laboratory (Sect. II F), and supporting material is left for the Appendices (Sect. V).

A. Hamiltonian and Unitary Transformation

SLBO are most easily studied using a coordinate system that is co-moving with the accelerating lattice [27–29], and a unitary transformation can be used to boost the Hamiltonian between the atom's inertial frame and the accelerating lattice frame [29, 30]. For DLBO, it is not possible to transform to a coordinate system that is simultaneously co-moving with both lattices. Instead, by using a basis of momentum states, each momentum state can be transformed independently so that positive (negative) momentum states are boosted to a coordinate system co-moving with the positively (negatively) accelerating lattice. This unitary transformation is shown to capture to core dynamics of DLBO.

We begin with a Hamiltonian containing the AC Stark shift of two superposed optical lattices that are far detuned from single-photon transitions (see Figure 2). Experimentally, the lattices are realized with one upward-propagating laser frequency ω_1 , and two downward-propagating frequencies $\omega_2 \pm \omega_m(t)$. We work in the frame of reference where $\omega_1 = \omega_2 = \omega$, and denote $\omega_{\pm} = \omega \pm \omega_m(t)$. The relative velocity of the two lattices is given by $v = \omega_m(t)/k$, where k is the wavevector of the laser defined as $k = \omega/c$. Two-photon transitions leave atoms in the same internal state but different external momentum states. After adiabatic elimination of the excited state, the Hamiltonian for an atom in these two optical lattices can be written as:

$$\begin{aligned} H_{\text{BBS}}(t) &= \frac{\hat{p}^2}{2m} + \frac{U_0}{2} \left(\cos \left[2k_+ \hat{x} + \int_0^t \omega_m(t') dt' + \phi_1 \right] \right. \\ &\quad \left. + \cos \left[2k_- \hat{x} - \int_0^t \omega_m(t') dt' + \phi_2 \right] \right) \\ &= \frac{\hat{p}^2}{2m} + U_0 \cos[2k\hat{x}] \cos \left[\int_0^t \omega_m(t') dt' + \phi_0 \right]. \quad (1) \end{aligned}$$

Constant terms are dropped in the second form, which will be used for analytics and simulation. The wavevectors $k_+ = \omega_+/c$ and $k_- = \omega_-/c$ are nearly identical to

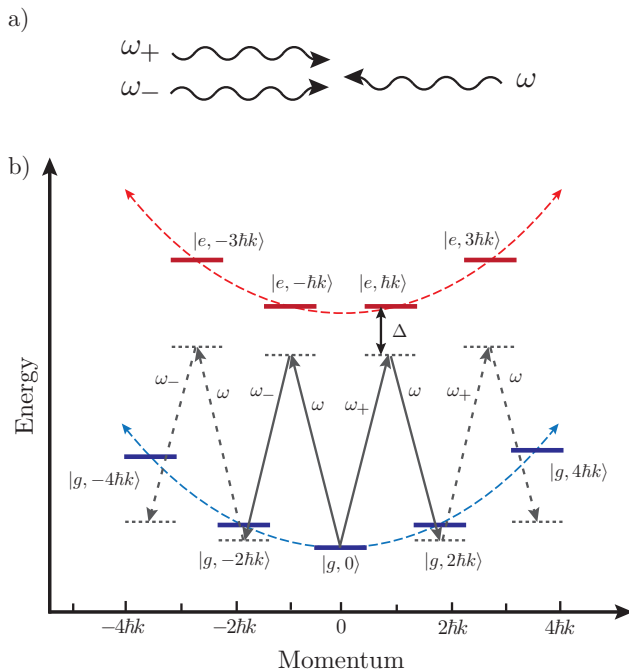


FIG. 2. a) Counter-propagating lasers form two superposed optical lattices. The frequency differences are $\omega_+ - \omega = \omega - \omega_- = \omega_m$. b) Energy-momentum level diagram showing relevant atomic states. The lasers drive two-photon transitions between neighboring momentum states such that the atom remains in the same internal ground state. The detuning from the excited states Δ (many GHz) is much larger than the separation between adjacent ground states (few kHz). As the modulation frequency ω_m is swept away from zero, the lasers sweep past a succession of two-photon transitions between adjacent ground states. Off-resonant transitions driven by the extra oscillating terms in Hamiltonian (4) are omitted for clarity.

k , so we approximate $k_+ \approx k_- \approx k$ in the second form as well. For Cs atoms separated by $n = 1000$ photon momenta, k_+ , k_- , and k differ by less than one part in 10^8 . The phases ϕ_0 , ϕ_1 and ϕ_2 are offsets between counter-propagating lasers at time $t = 0$. The lattice depth $U_0 = \hbar\Omega_R^2/2\Delta$ is the AC Stark shift for a single, far-detuned lattice [27], where Δ is the detuning from the excited state and Ω_R is the on-resonance Rabi frequency between the ground and excited states. The integral $\int_0^t \omega_m(t') dt'$ keeps track of the phase evolution of the lattice for time dependent frequencies. Specializing to linear frequency ramp rates r , the modulation frequency can be written as $\omega_m(t) = rt$ so that the lattices are velocity degenerate at time $t = 0$ and $\int_0^t \omega_m(t') dt' = rt^2/2$. This ramp rate corresponds to an acceleration $a = r/2k$.

We now write the Hamiltonian in a momentum-state basis $|l\rangle$, where l is an integer that labels the basis states such that the state $|l\rangle$ has $2l\hbar k$ momentum. Plane-wave basis states are a good approximation to initial atomic states when the velocity spread is much smaller than the recoil velocity $v_r = \hbar k/m$. Projected into this basis, the

Hamiltonian is:

$$H = \sum_{l=-\infty}^{\infty} \left(\frac{(2l\hbar k)^2}{2m} |l\rangle\langle l| + U_0 \cos\left(\frac{rt^2}{2} + \phi_0\right) (|l\rangle\langle l+1| + |l\rangle\langle l-1|) \right) \quad (2)$$

The unitary transformation used to boost the different momentum states in this Hamiltonian is given by:

$$U = \sum_{l=-\infty}^{\infty} e^{i\frac{d(t)|\hat{p}|}{\hbar}} e^{i\frac{\theta(t)}{\hbar}} |l\rangle\langle l| \quad (3)$$

where $d(t) \equiv at^2/2 + \phi_0/k$ and $\theta(t) \equiv ma^2t^3/6$. The first term corresponds to the position translation operator, and the absolute value sign ensures that positive momentum states are translated with the positive-moving lattice while negative momentum states are translated with the negative-moving lattice. The $d(t)$ term in Eq. (3) also absorbs the offset phase ϕ_0 into the definition of the basis states. The $\theta(t)$ in Eq. (3) corresponds to a global energy shift to each state such that the energy of the ground states co-moving with either of the lattices stays near zero at all times [30]. See Appendix V A for the analogous treatment of the SLBO Hamiltonian.

The transformed Hamiltonian $H' = UHU^\dagger + i\hbar\frac{dU}{dt}U^\dagger$ is:

$$H' = \sum_{l \neq 0} \left[\frac{(2|l|\hbar k - Ft)^2}{2m} |l\rangle\langle l| + \frac{U_0}{2} \left(1 + e^{is_l(rt^2+2\phi_0)} \right) |l\rangle\langle l+1| + \frac{U_0}{2} \left(1 + e^{-is_l(rt^2+2\phi_0)} \right) |l\rangle\langle l-1| \right] + \frac{(Ft)^2}{2m} |0\rangle\langle 0| + \frac{U_0}{2} \left(1 + e^{-i(rt^2+2\phi_0)} \right) (|0\rangle\langle 1| + |0\rangle\langle -1|) \quad (4)$$

where $s_l \equiv l/|l|$ is the sign of the momentum state, and the force $F = rm/2k$ is adapted from the standard treatment of SLBO [27].

The nearest-neighbor coupling terms proportional to $|l\rangle\langle l \pm 1|$ include both a stationary term and an oscillating term. In a two-level system, oscillating coupling terms of this type can be dropped under a rotating wave approximation (RWA) provided the terms time-average to zero on the relevant timescale of the dynamics. Here, the couplings between neighboring momentum states can be treated with an analogous RWA to arrive at the reduced DLBO Hamiltonian:

$$H_{\text{DLBO}} = \sum_{l=-\infty}^{l=\infty} \frac{(2|l|\hbar k - Ft)^2}{2m} |l\rangle\langle l| + \frac{U_0}{2} (|l\rangle\langle l+1| + |l\rangle\langle l-1|) \quad (5)$$

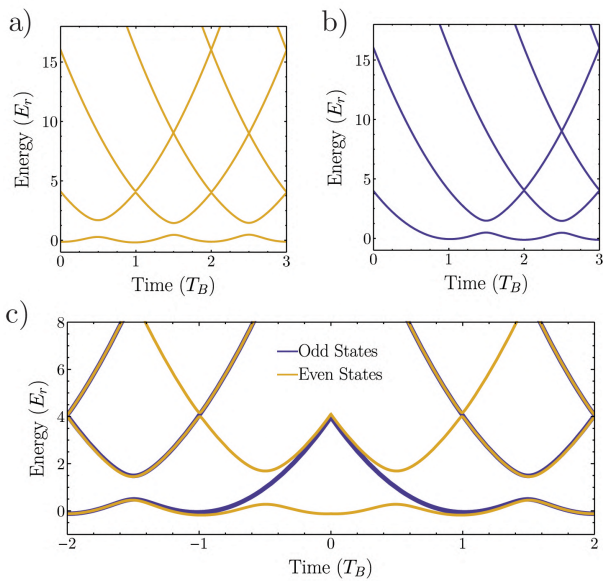


FIG. 3. Energy band structures of the reduced Hamiltonian (5) as a function of time, using a lattice depth $U_0 = 1E_r$. a) Even-parity and b) Odd-parity energy eigenvalues starting from velocity degeneracy. c) Combined band structure as lattices are ramped through velocity degeneracy at time $t=0$.

The validity of this RWA is discussed in Sect. II B, where we derive bounds on the ramp rate for which the Hamiltonian in Eq. (5) is valid.

The DLBO Hamiltonian in Eq. (5) and the SLBO Hamiltonian derived in Appendix V A are nearly identical; the only difference is the absolute value $|l|$ in the kinetic energy term for H_{DLBO} , which makes H_{DLBO} symmetric under momentum inversion. This symmetry is already obvious in the original Hamiltonian (1), which commutes with a momentum inversion operator. Using a basis of momentum eigenstates that are also eigenstates of momentum-parity, the even- and odd-parity states are decoupled.

Figure 3 (a,b) shows the energy band structure over time of the Hamiltonian (5) for even- and odd-parity states respectively, where the two lattices are ramped away from velocity degeneracy beginning at time $t=0$. The energy bands are calculated by finding eigenvalues of a truncated version of the Hamiltonian in Eq. (5) as a function of time. Note that in plotting the energy bands in Figure 3c, for negative times we use the substitution $d(t) \rightarrow -d(t)$ in Eq. (3) in order to use the coordinate frame co-moving with the lattices that drive amplitude towards zero momentum instead of driving amplitude away from zero momentum.

A Bloch beamsplitter can be understood as an atom adiabatically following the even-parity ground state of the Hamiltonian (5), and higher efficiency beamsplitters can be achieved by making the process more adiabatic. At every time $t = (m + 1/2)T_B$ for integer $m \geq 0$, there is a level crossing such that the even state receives an additional $4\hbar k$ momentum splitting; the positive momen-

tum component of the even state acquires an additional $+2\hbar k$ momentum and the negative momentum component acquires an additional $-2\hbar k$ momentum. This is the momentum-symmetric analogue of SLBO in the ground Bloch band, where atoms receive $2\hbar k$ momentum at the edge of the first Brillouin zone at each avoided level crossing between the ground band and first excited band.

B. Limits on Ramp Rate from the RWA

A RWA can be used to drop the oscillating coupling terms in Eq. (4) provided that the time-average of the oscillating term e^{irt^2} is $\ll 1$ on the relevant timescale of the dynamics. We take this timescale to be the duration of first level crossing between the ground even band and the first excited even band. Defining the Bloch period $T_B = 8\omega_r/r$ and the recoil frequency $\omega_r = \hbar k^2/2m$, the first level crossing between adjacent momentum states occurs at time $t = T_B/2$, and the time interval during which the level crossing happens is given by $\Delta t = 2\sqrt{2}U_0/\hbar r$. A simplified form of the resulting inequality gives an upper limit on the ramp rate for which the RWA is valid:

$$r \ll 4U_0(2\sqrt{2}E_r - U_0)/\hbar^2 \quad (6)$$

where we define the recoil energy $E_r = \hbar\omega_r$. The RWA is therefore valid in the limit as $r \rightarrow 0$. See Appendix V B for a full derivation of this condition as well as numerical simulation checking the validity of the RWA.

C. Limits on Ramp Rate from Landau-Zener Tunneling and Higher-Order Transitions

Non-adiabatic Landau-Zener losses arise from the level crossings in Figure 3 between the first and second even-parity energy bands. In SLBO, the survival probability per Bloch oscillation is given by $P_{LZ} = 1 - e^{-2\pi\Gamma_1}$ where $\Gamma_1 = U_0^2/4\hbar^2 r$ is the Landau-Zener parameter [31, 32]. For ramp rates $r < \omega_r^2$, this formula also describes losses from all level crossings of the DLBO Hamiltonian in Eq. (5) except the two level-crossings at $t = \pm T_B/2$. These two crossings between even-parity eigenstates have an additional factor of $\sqrt{2}$ in the energy gap, derived in Appendix V F. The Landau-Zener parameter Γ_2 for these two crossings is therefore given by $\Gamma_2 = U_0^2/2\hbar^2 r$. The dual-lattice beamsplitter is more robust to Landau-Zener losses at the first level crossing than SLBO at a fixed lattice depth U_0 , as shown in Figure 9.

Figure 4 shows the simulated efficiency of a single Bloch oscillation at a constant Landau-Zener parameter for both the SLBO and DLBO Hamiltonians in Eq. (2) and (7) respectively. These simulations are performed by numerically integrating the Schrodinger equation with the Hamiltonian in Eq. (2). Beginning with a free particle (plane-wave) momentum state, the simulation adiabatically loads the lattice, ramps the modulation frequency to its final value, then adiabatically unloads the

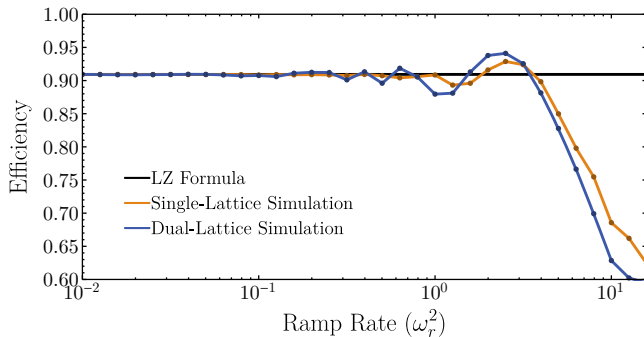


FIG. 4. Simulation of single-lattice and dual-lattice Bloch oscillation efficiencies for one level crossing. For each ramp rate, the lattice depth is chosen to keep the Landau-Zener parameters constant at $\Gamma_1 = \Gamma_2 = 0.3$ such that the expected losses from the Landau-Zener (LZ) formula are constant. See text for details.

lattice, and the efficiency is defined as the fraction of the population in the desired final momentum states. In order to have the same expected Landau-Zener losses for both simulations, the SLBO lattice depth is increased by a factor of $\sqrt{2}$ for each ramp rate compared to the DLBO simulation such that $\Gamma_1 = \Gamma_2 = 0.3$. There is asymptotic agreement with the Landau-Zener formula for ramp rates $r \ll \omega_r^2$ for both single-lattice and dual-lattice level crossings. There is additional oscillatory behavior of the DLBO efficiency compared to the SLBO efficiency owing to the oscillatory terms dropped in the RWA.

The rotating terms being dropped in the RWA can also contribute to higher-order processes that couple amplitude from the ground band to higher energy bands, and are further discussed in Appendix VC. The dominant loss channel is a third-order transition that couples the first and second energy levels around time $t = T_B/6$. These higher-order losses place a lower limit on the ramp rate, below which losses from the ground band begin to be appreciable.

D. Comparison of Limits on the Ramp Rate

The RWA condition in Eq. (6) and Landau-Zener tunneling losses both place an upper limit on the ramp rate. For Landau-Zener losses, efficient dynamics require $r \ll (\pi/2)U_0^2\hbar^2$; when $U_0 \lesssim \sqrt{2}E_r$, the RWA condition in Eq. (13) is automatically satisfied if the lattice depth is large enough to sufficiently suppress Landau-Zener tunneling. The RWA that leads to the Hamiltonian (5) is therefore asymptotically correct in the limit $r \rightarrow 0$ provided that $\hbar\sqrt{r} \ll U_0 \lesssim \sqrt{2}E_r$. On the other hand, when $U_0 \gtrsim \sqrt{2}E_r$, both the RWA condition and the standard Landau-Zener criterion begin to fail because the time windows for successive transitions begin to overlap non-negligibly.

Higher-order losses place a lower limit on the ramp rate, and for $r \leq \omega_r^2$, this limit and the upper limits on

the ramp rate from Landau-Zener losses and the RWA condition can all easily be satisfied. Because of the non-linear scaling of these different limits on the ramp rate, the maximum possible efficiency of the processes quickly approaches 1 as $r \rightarrow 0$; for $r = 0.5\omega_r^2$, the maximum efficiency of the initial $4\hbar k$ momentum splitting in a Bloch beamsplitter is already $> 99\%$.

E. Crossing through velocity degeneracy

In addition to a beamsplitter, one can also ramp the two lattices through velocity degeneracy to create atom mirrors and combiners. This process has previously been attempted experimentally [33], but the dynamics were seen to be very inefficient without optimizing the ramp rate, lattice depth, and relative phase between lattices. Figure 3c shows the band structure for negative times as well as positive times as the lattices are ramped through velocity degeneracy at time $t = 0$. Far from velocity degeneracy, the even and odd ground state energy bands overlap and have the same level crossing structure. Near time $t = 0$, however, these energy bands deviate because an odd-parity state in momentum space cannot have amplitude on the zero-momentum basis state $|0\rangle$. As a result, the odd-parity ground state has no level crossing coupling momentum into the zero momentum state, so the even parity ground state passes through two additional level crossings compared to the odd parity ground state when crossing through velocity degeneracy.

One arm of an interferometer can be decomposed into a superposition of two ground states, one of even and one of odd parity, when the arm is initially co-moving with one of the two lattices. Relative phase shifts between the even and odd states causes amplitude to add constructively on positive or negative momentum states, as discussed in detail in Appendix IIE. The relative phase ϕ_0 of the two optical lattices is added to the even-parity state wavefunction as a laser phase during these two level crossings, and as a result the offset phase ϕ_0 coherently controls the population in the two lattices after a degeneracy crossing. This allows one to create reflection or recombination pulses in an interferometer, and together with the beamsplitter process described previously, this comprises a full set of atom-optics tools for atom interferometry (see Figure 6 for experimental implementation).

F. Experimental Considerations

The dynamics are sensitive to the initial velocity distribution of an atom. Numerical integration of the Hamiltonian (1) can be used to solve for evolution of a wavefunction $\psi(x, t)$ with arbitrary initial conditions (see figure 1). These simulations are based on algorithms outlined in reference [34], and implemented numerically using fast linear algebra methods in the programming language Julia. Efficient dynamics are observed for atoms with co-

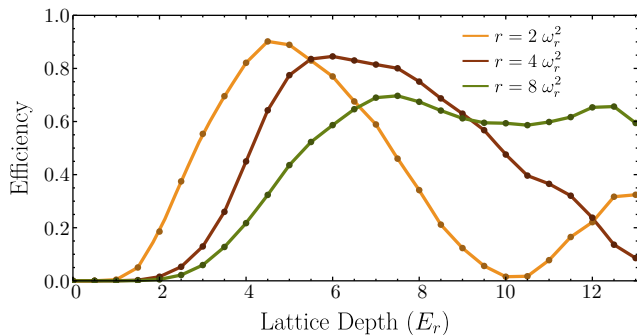


FIG. 5. Numerical simulation of beamsplitter efficiency performed with momentum space basis. The simulation includes adiabatic loading of lattice, frequency ramping for four Bloch periods, and adiabatic unload, such that the final momentum splitting is $16\hbar k$. Efficiency is defined as the probability amplitude on the desired momentum states after unloading the lattice. See text for discussion of loss mechanisms.

herent velocity spreads of more than $\sigma_v = 0.5v_r$, where σ_v is the standard deviation in velocity of a Heisenberg limited Gaussian wavefunction, in agreement with results in reference [21] for coherent velocity distributions. The fraction of the wavefunction lost from the ground band is consistent with the portion of the wavefunction amplitude initially outside of the first Brillouin zone ($-v_r, v_r$). The center of the distribution has been assumed to be at zero velocity.

If the center of the atomic velocity distribution is non-zero, the initial state has some projection onto the odd-parity eigenstates when loaded into the lattice, leading to asymmetry and diffraction phases. Diffraction phases are fundamental to any asymmetric Bragg diffraction beamsplitter [35, 36], and must be accounted for in precision measurements [1]. The symmetry of the Bloch beamsplitter (see Figure 1) ensures that there is no diffraction phase that is fundamental to the technique. An initial velocity of the atoms, however, breaks the symmetry and creates a diffraction phase between interferometer arms. A numerical study of the diffraction phase associated with missing the center velocity is discussed in Appendix VE, which shows that there are magic lattice depths that result in a suppression of the diffraction phase. For realistic experimental parameters, the diffraction phase can be limited to ± 10 mRad independent of the momentum splitting. Increasing the momentum splitting will therefore fractionally suppress the diffraction phase, and diffraction phases can also be measured directly by varying the T of an interferometer. Note also that an ensemble of atoms with different center velocities will result in phase spreading in an interferometer.

The analytic results derived above only apply to slow ramp rates that satisfy the condition in Eq. (6). Experimentally, we use ramp rates as large as $r = 10\omega_r^2$ and lattice depths around $8E_r$ in order to maximize interferometer contrast, which is a region of parameter space

that breaks the assumptions used to derive this inequality. Although the analytical efficiency predictions break down in this regime, we still observe reasonably efficient dynamics both numerically and experimentally. Some numerical efficiency curves for a Bloch beamsplitter are illustrated in Figure 5. Losses at low lattice depths on these curves are from Landau-Zener tunneling from level crossings. Losses at high lattice depths are from high-order transitions coupling amplitude into higher bands, and if the lattice depth is further increased, additional higher-order transitions can couple amplitude back into the ground band resulting in oscillations in the efficiency curves as seen in the $r = 2\omega_r^2$ curve in Figure 5.

III. EXPERIMENT

Our experimental apparatus has been described previously [1]. A magneto-optical trap of Cesium atoms is launched vertically in an atomic fountain. The cloud is further cooled to a few hundred nK using polarization gradient cooling and Raman sideband cooling. Three successive Raman transitions prepare the atom in the internal state $|F = 3, m_F = 0\rangle$ with a vertical velocity spread around 0.05 recoil velocities v_r .

The frequencies ω_1 and ω_2 in the Hamiltonian (1) are ramped in the lab to compensate for Doppler shifts from gravitational acceleration of the atoms such that in the atom's inertial frame, $\omega_1 = \omega_2 = \omega$. The optical lattice is detuned by +80 GHz (blue) from the Cs D2 line, and is formed from a roughly Gaussian beam with $1/e$ waist of about 3 mm that is retroreflected. The frequency components ω_1 and $\omega_{2\pm}$ are cross polarized and a quarter waveplate is placed in front of the retroreflecting mirror such that the desired lattices are formed upon retroreflection. The laser intensity is actively stabilized by feeding back to the drive power of an acousto-optic-modulator (AOM) [37].

The modulation frequency $\omega_m(t)$ from the Hamiltonian in Eq. 1 determines the velocity splitting between the two lattices. It is generated experimentally by mixing the output of an AD9959 digital frequency synthesizer with a 10 MHz clock and low-pass filtering the output, after which $\omega_m(t)$ is mixed into the drive frequency for an AOM to generate frequency sidebands that are written onto the laser. The offset phase ϕ_0 is a tuneable parameter on the digital frequency synthesizer.

To create a Bloch beamsplitter, atoms are adiabatically loaded into two velocity-degenerate lattices that initially add constructively to form a single lattice, which corresponds to $\omega_m = 0$ and $\phi_0 = 0$ at time $t = 0$ in Eq. (1). The modulation frequency is then ramped linearly at a rate r such that $\omega_m = rt$ and the two lattices accelerate away from one another. The resulting momentum distribution is then measured using time-of-flight detection, as shown in Figure 1b. The final atomic state after the beamsplitter is mostly in the $|\pm n\rangle$ states, with a small number of atoms left in the $|0\rangle$ state.

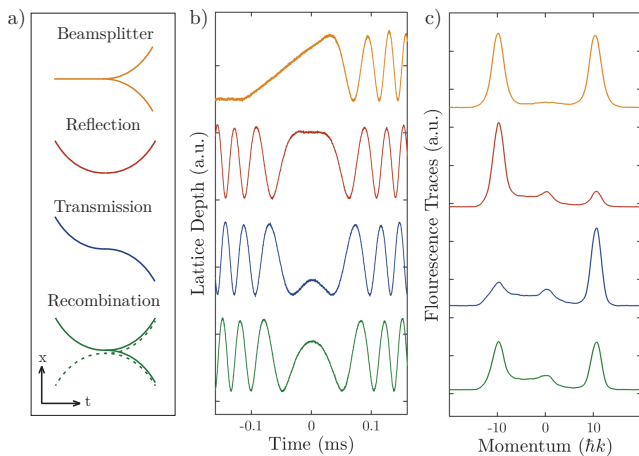


FIG. 6. Experimental realization of a Bloch beamsplitter (yellow), reflection (red), transmission (blue), and recombination (green) as lattices are ramped through velocity degeneracy. a) Space-time trajectories. b) Intensity profiles of the $\omega_2 \pm \omega_m(t)$ interferometry beams, which are measured by imaging the laser beams on a photodiode just before entering the vacuum chamber. The profiles show beats between the two frequencies, which is the temporal part of the potential in the Hamiltonian (1). Time $t = 0$ indicates when $\omega_m = 0$. Different phase offsets ϕ_0 result in different beat profiles on the beam. c) Fluorescence traces of atoms from time-of-flight imaging showing the resulting distribution after various operations.

In addition to an initial beamsplitter, a full interferometer sequence requires reflection pulses to reverse momentum of the interferometer arms and a recombination pulse to interfere the two arms together. In Section II E, it was shown that the phase ϕ_0 in the Hamiltonian in Eq. (1) can be used as a parameter to coherently control the output nature of the degeneracy crossing. This phase also controls the interference (“beat”) between the two optical lattices at the crossing, as shown in Figure 6b. Varying ϕ_0 from 0 to π controls the population in the two lattices after the degeneracy crossing from reflection to transmission, with a beamsplitter/recombination behavior at an intermediate ϕ_0 . These phases are varied experimentally and the optimal phase offsets ϕ_0 are found which maximize population in the desired output channels, as shown in Figure 6. Note that the optimal phase offset ϕ_0 is dependent on both the ramp rate and the lattice depth U_0 ; the beat profiles shown in Figure 6b are specific to the lattice depth and ramp rate used experimentally, and will need to be optimized anew if either parameter is changed. This is due to the fact that the dynamical phase ϕ_d in Eq. (15) is a function of both the ramp rate and the lattice depth. For the parameters used in our experiment, the simulated efficiencies are similar to those realized experimentally, but experimentally we see more atoms lost to the zero momentum state.

Combining these techniques, we implement a MZ interferometer, see Figure 7. The sequence starts with a Bloch beamsplitter that is ramped to some final momen-

tum splitting n_i . After this, a reflection sequence is performed and the phase ϕ_0 in the Hamiltonian Eq. (1) is arranged as shown in Figure 6b. The two halves of the wavefunction are then interfered using a recombination sequence and the outputs are separated to some final momentum state n_f .

To optimize the contrast of the detected interferences, we need to make sure that the detected atoms are separate from background atoms that arise from loading and unloading the lattices. Using $n_f > n_i$ separates “signal” atoms from those backgrounds in time-of-flight imaging, see Figure 7b.

A ramp rate for ω_m of $r/(2\pi) = 249$ MHz/s and a lattice depth around 8 recoil energies are used as these parameters resulted in the largest interferometer contrast. The phases ϕ_0 for the two degeneracy crossings are also optimized experimentally to maximize contrast. In between different interferometer operations, we switch the direction of the modulation frequency ramp by switching RF frequency sources for the modulation frequency $\omega_m(t)$, and we adiabatically unload the lattice during this time to avoid losses from the ground state.

We observe up to 40% contrast in a $T = 8.5$ -ms, $20\hbar k$ interferometer where atoms are guided in the lattices during 16.7 ms of the 17 ms interferometer duration (Figure 7e). Since there is vibration noise in the experiment, it is not possible to observe a stable fringe, so contrast is determined by measuring the fluctuations in the output populations on a histogram. Without changing the laser intensity profile, momentum transfer is increased by changing the profile of ω_m as shown in Figure 7a, and contrast is observed up to $240\hbar k$ momentum splitting.

Observing contrast in an interferometer does not ensure that the interferometer is phase-stable. In order to show phase-stability and first-order coherence [38], we also perform a differential measurement between two MZ interferometers in a gradiometer configuration, see Figure 8. In this configuration, phase noise from vibrations is common to both MZ interferometers, so the differential measurement can reveal a stable relative phase. The two MZ interferometers are separated vertically by roughly 11 cm by using a $500\hbar k$ Bloch beamsplitter with a ramp rate of $r/(2\pi) = 51$ MHz/s. Within each MZ, a momentum splitting of $20\hbar k$, an interferometer time $T_i = 10$ ms, and a ramp rate of $r/(2\pi) = 249$ MHz/s are used. The slower ramp rate for the first beamsplitter minimizes background atoms in the time-of-flight traces, and the faster ramp rate during the interferometer maximizes contrast. Phase-stability is observed between the interferometers by plotting the relative populations parametrically (see Figure 8b).

If there is no differential phase acquired between the interferometers, as is the case for $\delta T = 0$ (δT is defined in Figure 8a), we see perfect correlation in the outputs, and common-mode vibration noise causes data to fall at different points on this line. Differential phase shifts between the two MZs results in an elliptical distribution; by delaying the final pulse, a phase difference is intro-

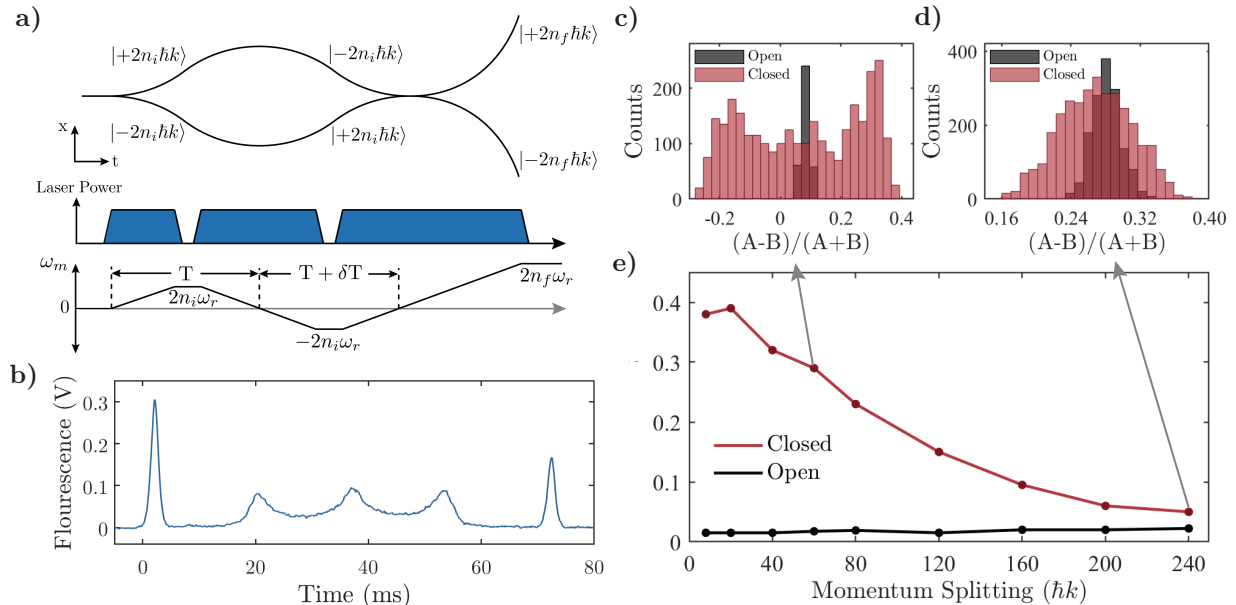


FIG. 7. Experimental realization of a Mach-Zehnder interferometer. a) Interferometer geometry, laser intensity profile, and profile of the modulation frequency ω_m vs. time. The time interval T is defined based on ω_m -zero crossings. A time offset can be used to open the interferometer to eliminate interference, while $\delta T = 0$ leads to maximum contrast. b) Sample fluorescence trace of a $T = 8.5$ ms, $60\hbar k$ MZ interferometer. c,d) Histogram of population fractions for $60\hbar k$ and $240\hbar k$ momentum splittings, respectively, in $T = 8.5$ ms interferometers. Population fraction is defined as $(A - B)/(A + B)$ where A and B are populations in the two output ports. e) Contrast versus momentum splitting for closed and open interferometers.

duced between the interferometers such that the parametric plot becomes an ellipse. Differences in gravity between the two MZs also create a differential phase shift which is proportional to the gravity gradient. However, this phase is around 5 mrad for the parameters used experimentally and is too small to be observed. The phase coherence between the two MZs demonstrates that the technique is first-order coherent and phase-stable, and can therefore be used for measurements in atom interferometry. We achieve as large as 50% contrast in the differential measurement, which is similar to the largest contrast we ever observed with Bragg diffraction in the same instrument. The contrast is higher than the contrast in the Mach-Zehnder interferometers in Figure 7 because the lattice in the gradiometer configuration is turned off when the lattices are not being accelerated. The timing delay causes loss of contrast because of not fully closing the interferometer, and we do not yet have an explanation for why the timing delay introduces a phase difference.

IV. CONCLUSIONS AND OUTLOOK

We have developed new techniques for coherently manipulating atomic wavefunctions by generalizing Bloch oscillations to two independently accelerated optical lattices near velocity degeneracy. First, the Hamiltonian was treated analytically, and it was shown that the dy-

namics can produce efficient and coherent atom optics elements. For slow ramp rates, the process is adiabatic and atoms can adiabatically follow the even-parity ground state of Hamiltonian (5). When ramping lattices through velocity degeneracy, the populations in the two lattices can be controlled by changing the relative phase of the two optical lattices, allowing for all atom-optics elements required to form an interferometer. Combining these techniques, a MZ interferometer was created that showed contrast at up to $240\hbar k$ momentum splitting, one of the largest splittings achieved to date in an atom interferometer. Phase stability was demonstrated with a differential measurement, showing that the techniques are first-order coherent and can be used for measurement.

There are a number of advantages to using Bloch beamsplitters and dual-lattice methods over existing techniques, and applications with constraints on laser power and free-fall distance, such as space based interferometry [39, 40] or portable atomic gravimeters [10], can benefit from these techniques by maximizing momentum transfer in the constrained system. First, being based on adiabatic processes, these methods can be robust to fluctuations in experimental parameters like lattice depth or laser frequencies [27] and allow for a larger velocity class of atoms to undergo efficient dynamics. Resonant Bragg diffraction restricts the velocity class of atoms that can be diffracted, and this restriction scales inversely with the momentum splitting [15]. On the other hand, the adiabatic Bloch beamsplitter produces efficient dynam-

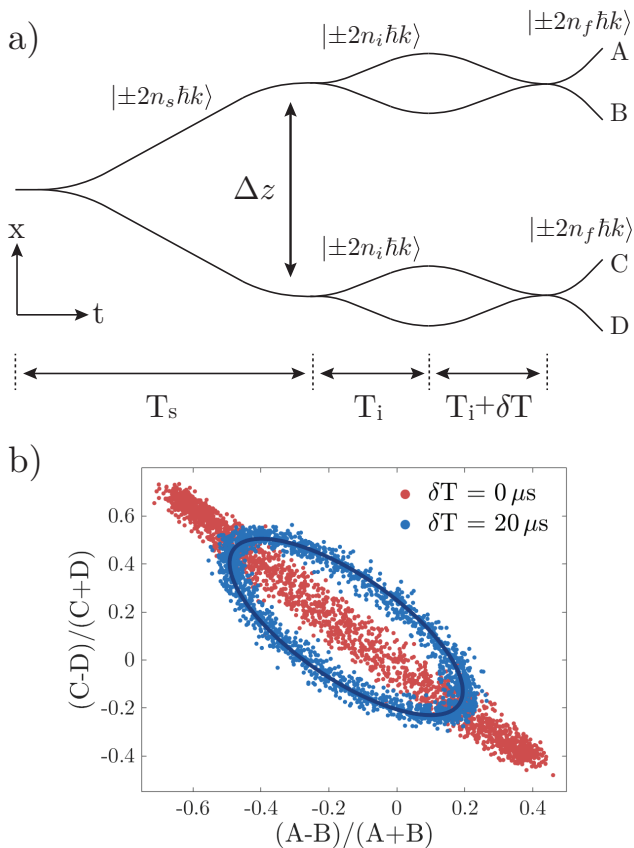


FIG. 8. a) Schematic of a dual-lattice gradiometer. A and B are populations in output ports of one MZ, and C and D are populations in output ports of the second MZ. b) Parametric plot of data taken using $n_s = 125$ and $T_s = 150$ ms for $\Delta z \approx 11$ cm vertical splitting between the two MZ interferometers. Within the interferometers, $n_i = 5$ and $T = 10$ ms, and $n_f = 10$ to resolve the outputs. The dark line is an ellipse fit to the $\delta T = 20 \mu\text{s}$ data.

ics for any velocity width inside of the first Brillion zone, independent of the final momentum splitting, so these methods relax the atomic temperature requirements in an experiment. The laser power required for higher-order Bragg diffraction scales quadratically with the momentum splitting, whereas the laser power required for Bloch beamsplitters is independent of the momentum splitting, relaxing the laser power requirements in an experiment.

Compared to combinations of Bragg diffraction and Bloch oscillations [22, 23], the dual-lattice processes require less laser power and can achieve higher efficiencies. For example, two sequential $4\hbar k$ double-Bragg beamsplitters used in reference [13] use a peak lattice depth of $3 - 4E_r$ and achieve a total efficiency around 90%, and higher-order double Bragg pulses require considerably more laser power. In contrast, the $60\hbar k$ beamsplitter in Figure 1b uses a lattice depth of $1.5E_r$ while achieving an efficiency greater than 90%. Double-Bragg pulses can be made more efficient with longer duration pulses, but this restricts the velocity width that can undergo efficient

dynamics. In contrast, the Bloch beamsplitter and dual-lattice methods can be made as efficient as necessary by ramping more slowly and using lower laser power without placing any further restrictions on the velocity width of atoms.

A generalization of these dual-lattice techniques shows promise for new measurements of the fine-structure constant α . By removing the assumption that $\omega_1 = \omega_2$ and are independent of time in the Hamiltonian in Eq. (1), asymmetric lattice guided geometries can be created as was investigated in [30]. Differential accelerations between interferometer arms create a phase term in the interferometer that is proportional to m/\hbar , instead of \hbar/m . For realistic experimental parameters, one could obtain 10^{10} radians of phase in determining m/\hbar in an experimental apparatus similar to the one used in this experiment. This would increase the sensitivity to recoil phase by three orders of magnitude compared to the current leading measurement of α [1], and could be used for a next-generation measurement of α [30]. Another generalization of the Bloch beamsplitter uses a multi-photon, $4n\hbar k$ transition to open the interferometer where $n > 1$. Our numerical simulations show that this multi-photon process also leads to an efficient beamsplitter for appropriate ramp rates and lattice depths, see Appendix V C for further discussion.

Lastly, Bloch oscillations [41] and Bragg diffraction [42] were both originally studied in periodic solid state systems, and were only later extended to atoms in optical lattices. Dual-lattice Bloch oscillations, identified here for application to atoms in optical lattices, are a general solution to the scalar particle 1-D Schrödinger equation. These solutions could be extended to solid state systems as well with an appropriately engineered solid-state potential.

The authors would like to thank Matt Jaffe, Victoria Xu, Sven Abend, Ernst Rasel, Justin Khoury and Tanner Trickle for useful discussions and feedback, as well as the past group members who helped develop the experimental apparatus including Brian Estey, Joyce Kwan, Chenghui Yu, Pei-Chen Kuan, and Shau-Yu Lan. This work was supported by the National Science Foundation Grant No. 1806583, the National Institute of Science and Technology Grant No. 60NANB17D311, and the W.M. Keck Foundation Grant No. 042982. Z.P. acknowledges funding from the National Science Foundation GRFP.

V. APPENDICES

A. Unitary transformation for single-lattice Bloch Hamiltonian

In an inertial frame initially co-moving with the atoms, the SLBO Hamiltonian can be written as:

$$H = \sum_{l=-\infty}^{\infty} \left(\frac{(2l\hbar k)^2}{2m} |l\rangle\langle l| + U_0 e^{i\left(\frac{rt^2}{2} + \phi_0\right)} (|l\rangle\langle l+1| + |l\rangle\langle l-1|) \right) \quad (7)$$

The Hamiltonian in Eq. (10) in the main text is derived by transforming this Hamiltonian, Eq. (7), into a rotating frame that puts the time dependence of the rotating terms into the diagonal. This is achieved with the following unitary:

$$U = \sum_{l=-\infty}^{\infty} e^{i\frac{d(t)\hat{p}}{\hbar}} e^{i\frac{\theta(t)}{\hbar}} |l\rangle\langle l| \quad (8)$$

$$= \sum_{l=-\infty}^{\infty} e^{il\left(\frac{rt^2}{2} + \phi_0\right)} e^{i\frac{ma^2t^3}{6\hbar}} |l\rangle\langle l| \quad (9)$$

with $d(t) \equiv at^2/2 + \phi_0/k$ and $\theta(t) \equiv ma^2t^3/6$. This same transformation is used in reference [43], and it is almost identical to the transformation used in Eq. (3), except there is no longer a absolute value sign on the momentum operator. Acting on the Hamiltonian in Eq. (7) with the unitary transformation in Eq. (8) results in H_{SLBO} :

$$H_{\text{SLBO}} = \sum_{l=-\infty}^{\infty} \frac{(2l\hbar k - Ft)^2}{2m} |l\rangle\langle l| + \frac{U_0}{2} (|l\rangle\langle l+1| + |l\rangle\langle l-1|) \quad (10)$$

The Ft term that appears in the kinetic energy is related to the quasimomentum k_q through the relation $\hbar k_q = Ft$.

B. RWA Condition

To make the rotating wave approximation (RWA) in Eq. (4), we average the oscillating term e^{irt^2} over the time it takes for the transition between momentum states to take place. This term is oscillating most slowly around the first level crossing between the first and second even bands at time $t = T_B/2$. In the limit of small lattice depths $U_0 \ll 4E_r$, the energy gap $E_g(t)$ near this level crossing is given by:

$$E_g(t) = \sqrt{\hbar^2 r^2 (t - T_B/2)^2 + 2U_0^2} \quad (11)$$

such that the center of the level crossing occurs at time $t = T_B/2$, and the duration of the level crossing is $\Delta t = 2\sqrt{2}U_0/\hbar r$.

Taking the time average of the rotating term e^{irt^2} over the duration of the level crossing gives the following:

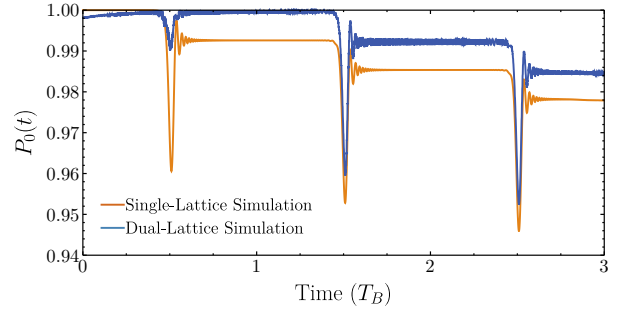


FIG. 9. Probability amplitude in the ground state over three Bloch periods for single-lattice and dual-lattice simulations. A lattice depth of $U_0 = 0.5E_r$ and ramp rate $r = 0.02\omega_r^2$ are used for both simulations. The lattice depth is intentionally chosen to be low in order to illustrate loss mechanisms for SLBO in comparison with DLBO. See text for discussion.

$$\langle e^{irt^2} \rangle \approx -\frac{i\hbar^2 r}{4U_0} e^{i\alpha} \frac{U_0 \cos \beta - 2\sqrt{2}iE_r \sin \beta}{8E_r^2 - U_0^2} \quad (12)$$

where $\alpha = 2(8E_r^2 + U_0^2)/\hbar^2 r$, $\beta = 8\sqrt{2}E_r U_0/\hbar^2 r$, and we have assumed that $r \ll 2(2\sqrt{2}E_r - U_0)^2/\hbar^2$. The rotating term can be dropped so long as this average is small compared to 1, i.e., when

$$|\langle e^{irt^2} \rangle| < \frac{\hbar^2 r}{4U_0(2\sqrt{2}E_r - U_0)} \ll 1 \quad (13)$$

or equivalently, $r \ll 4U_0(2\sqrt{2}E_r - U_0)/\hbar^2$. We note that varying the time window of integration in Eq. (12) changes the numerical prefactors in Eq. (13), but not the limiting behavior as $r \rightarrow 0$.

The validity of the RWA can further be studied with numerical simulation. By solving for the evolution of $|\psi(t)\rangle$ from the Hamiltonian in Eq. (4), the full state evolution is captured without utilizing the RWA. This state evolution can then be compared with the eigenstates of the Hamiltonian in Eq. (5) after applying the RWA. When the condition in Eq. (13) is satisfied, the general state evolution $|\psi(t)\rangle$ follows the ground state of the reduced Hamiltonian in Eq. (5) very closely. Figure 9 shows the probability amplitude in the ground state of Eq. (5) over time, defined as $P_0(t) = |\langle +_{gs}(t) | \psi(t) \rangle|^2$. The state $|+_{gs}(t)\rangle$ denotes the even-parity ground state of Hamiltonian (5) as a function of time. For this simulation, the atom begins in the ground state of the two lattices at time $t = 0$ with $\omega_m(t = 0) = 0$ and $\phi_0 = 0$, after which $\omega_m = rt$ to ramp the lattices apart.

Figure 9 shows that the eigenstates of the Hamiltonian in Eq. (5) are nearly identical to the true state evolution under the Hamiltonian in Eq. (2). To stress the parallel between SLBO and DLBO, we also plot the probability amplitude in the ground state for SLBO using eigenstates calculated from the Hamiltonian in Eq. (10). In both simulations, the states pass avoided level crossings

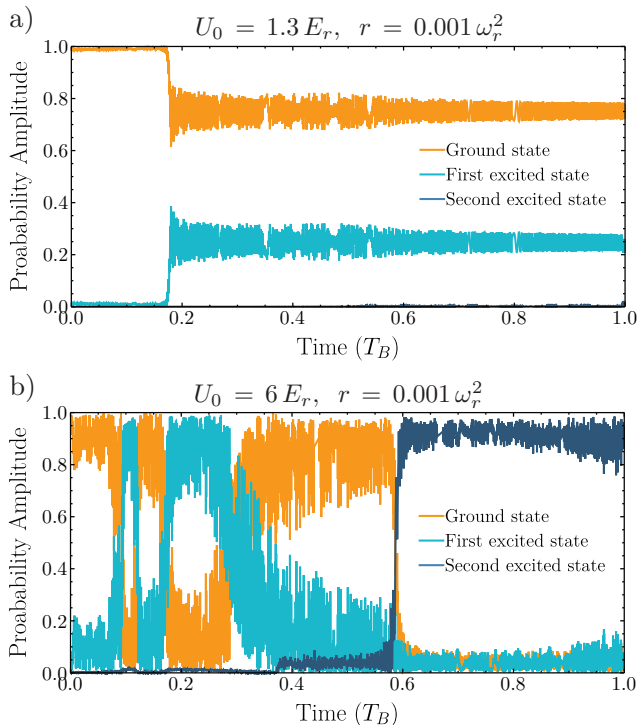


FIG. 10. Simulations of one Bloch period of a Bloch beamsplitter illustrating losses from the ground band due to higher-order transitions. The states used for determining the probability amplitude are even-parity eigenstates of Hamiltonian (5). A slow ramp rate is used so that the various transitions are resolved from one another. a) The first losses to occur are due to a third-order transition coupling the ground state and first excited state. b) A much larger lattice depth shows a number of different higher-order transitions. Before time $t = T_B/2$ there are four separate higher-order resonances between the ground state and first excited state that transfer population between the levels. Around time $t = 0.6 T_B$ there is a transition between the ground state and the second excited state.

at times $t = (m + 1/2)T_B$ for integer m . At each crossing there is mixing with the second band, and Landau-Zener tunneling losses lead to a loss of probability amplitude from the ground state. The energy gap for the first level-crossing in DLBO is larger than the subsequent gaps by a factor of $\sqrt{2}$, so there is less mixing and less tunneling during the first level crossing for DLBO compared to the SLBO. The dual-lattice simulation doesn't project perfectly onto the ground eigenstate around time $t = 0$ due to the perturbation terms dropped in the RWA.

C. Higher-order loss mechanisms

When the lattice depth is too large, the oscillating terms dropped in the rotating wave approximation from the Hamiltonian in Eq. (4) can contribute to higher-order parasitic transitions. The dominant loss mechanism at ramp rates $r \ll \omega_r^2$ is a third-order (six-photon) process

coupling the states $|0\rangle$ and $|+1\rangle$ around time $t = T_B/6$. There are two possible energy and momentum conserving pathways for the transition to occur; $|0\rangle \rightarrow |+1\rangle \rightarrow |0\rangle \rightarrow |+1\rangle$ and $|0\rangle \rightarrow |+1\rangle \rightarrow |+2\rangle \rightarrow |+1\rangle$. For lattice depths much less than the spacing between energy levels, $U_0/2 \ll 4E_r$, the effective coupling between these states scales like $(U_0/2)^3/(4E_r)^2$, which is the same scaling as the Rabi frequency in higher-order Bragg diffraction [15, 44].

During a Bloch beamsplitter, the laser frequencies are swept across this parasitic resonance, as seen in Figure 10a, which can be thought of as a parasitic level-crossing between $|0\rangle$ and $|+1\rangle$; for an efficient Bloch beamsplitter, amplitude should remain in $|0\rangle$ by tunneling through this level-crossing diabatically. To first-order, the adiabatic population transfer to the state $|+1\rangle$ during this level crossing is given by $P_{LZ} = 1 - e^{-2\pi\Gamma} \approx 2\pi\Gamma$ when the Landau-Zener parameter Γ is close to zero. For $U_0 \ll 8E_r$ and $r \ll \omega_r^2$, we therefore expect losses from the Bloch beamsplitter $P_{\text{loss}} = 2\pi\Gamma_3 \propto \frac{\omega_r^2}{r} \left(\frac{U_0}{8E_r}\right)^6$ where $\Gamma_3 \propto \frac{\omega_r^2}{r} \left(\frac{U_0}{8E_r}\right)^6$. This scaling of the higher-order losses in the limit of $r \rightarrow 0$ agrees with our numerical simulations.

In addition to the third-order process discussed above, there are an infinite number of these higher-order processes that conserve energy and momentum, but the transition rates are highly suppressed at lower lattice depths. Figure 10b illustrates what happens when the lattice depth is increased to a regime in which many of these higher-order transitions can couple amplitude to higher-excited states. The parameters chosen for this simulation happen to drive five of these higher-order transitions within the first Bloch period. A ramp rate $r \ll \omega_r^2$ is chosen for the simulation so that the transitions are well-resolved. In contrast, Figure 9 illustrates negligible higher-order losses because all higher-order transitions are highly suppressed at lower lattice depths.

D. Crossing through velocity degeneracy

The dynamics of one arm of an interferometer while crossing through velocity degeneracy is determined by phase shifts picked up to the parity eigenstates. An initial momentum state $|n\rangle$ can be decomposed as

$$|n\rangle = \frac{1}{\sqrt{2}}(|+n\rangle + |-n\rangle) \quad (14)$$

where $|+n\rangle = (|n\rangle + |-n\rangle)/\sqrt{2}$ and $|-n\rangle = (|n\rangle - |-n\rangle)/\sqrt{2}$ are the symmetric and antisymmetric combinations of the free-space momentum basis states $|\pm n\rangle$ derived in Appendix V F. For dual lattices that are initially co-moving with the states $|\pm n\rangle$, this state will be loaded into the ground state of the DLBO Hamiltonian in Eq. (5) as a superposition of odd-parity and even-parity ground states. Relative phase shifts between the

even and odd eigenstates causes amplitude to add constructively or destructively for the positive momentum or negative momentum states.

There are two sources of relative phase shifts between these states as the states are swept through velocity degeneracy. First, a dynamical phase difference ϕ_d between the two states given by $\phi_d = (1/\hbar) \int dt' (E_-(t') - E_+(t'))$, where E_{\pm} denotes the energy of the even- and odd-parity ground states as shown in Figure 3c. In addition, the two level crossings for the even state near velocity degeneracy add laser phase only to the even state. This laser phase can be controlled by varying the phase term ϕ_0 in the Hamiltonian in Eq. (1). Since there are two level crossings, the even state will receive a laser phase shift $\phi_l = 2\phi_0$. Formally, this can be seen from the definition of the unitary transformation in Eq. (3). As mentioned previously, the sign on $d(t)$ in Eq. (3) is changed at time $t = 0$, which redefines the phase convention on every basis state except for the zero momentum state $|0\rangle$. At time $t = 0$, the odd-parity ground state $| -_1 \rangle = (|1\rangle - |-1\rangle)/\sqrt{2}$ is therefore phase shifted by $2\phi_0$ compared to the state $|0\rangle$. This is not physical, but rather an artifact of our conventions for the unitary transformations. Physically, this phase is coming from the two level crossings of the even-parity state. This phase shift can also be observed in numerical simulations.

Up to a global phase, the new state after the degeneracy crossing can be written as:

$$|\psi_f\rangle = \frac{1}{\sqrt{2}}(e^{i(\phi_d + \phi_l)} |+_n\rangle + |-_n\rangle) \quad (15)$$

By controlling the phases ϕ_d and ϕ_l in an experiment, one has control over the output nature of the degeneracy crossing. For example, arranging for $\phi_d + \phi_l = 2m\pi$ for some integer m ensures that the state after the crossing will be identical to the state before the crossing, which corresponds to transmission through the crossing. For $\phi_d + \phi_l = (2m + 1)\pi$ for some integer m , the output state becomes $-|+_n\rangle + |-_n\rangle = |-_n\rangle$, which has opposite momentum compared to the input state $|n\rangle$ and corresponds to a reflection. Intermediate values of the phase can be used to split amplitude between the two momentum states $|\pm n\rangle$. In practice, it is easiest to change ϕ_0 , and therefore ϕ_l , since this phase is directly controllable experimentally. Our simulations show that ϕ_d also depends on ϕ_0 at the moment that the lattices are velocity degenerate, but this dependence does not prevent one from continuously transforming between different output behaviours by changing only ϕ_0 .

In the limit $U_0 = 0$, the dynamical phase ϕ_d is given by $\phi_d = 16\omega_r^2/r$, such that $\phi_d \gg 2\pi$ when $r \ll \omega_r^2$. When $U_0 > 0$, this phase term is also a function of the lattice depth; as a result, fluctuations in U_0 lead to fluctuations in ϕ_d , and variable U_0 across a finite laser beam leads to a variable ϕ_d across an atom cloud. Both of these effects result in unreliable zero-crossing behaviour at slow ramp rates. The latter is likely the reason that we see the largest interferometer contrast for $r = 10\omega_r^2$, as our

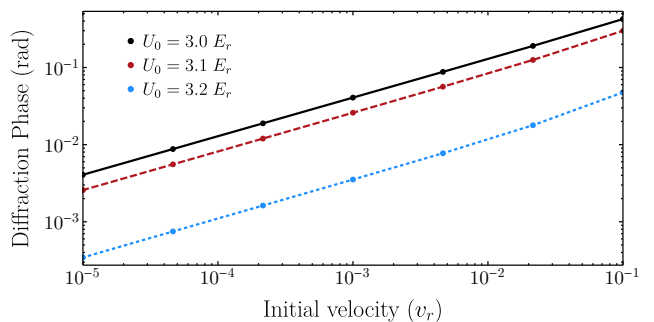


FIG. 11. Numerical simulation of diffraction phase from a Bloch beamsplitter as a function of velocity with respect to the initial optical lattice. Simulation includes adiabatically loading the lattice, frequency ramping at a rate $r = 1.0 \omega_r^2$ for four Bloch periods, then adiabatic unloading of the lattice. See text for further discussion.

laser beam waist is comparable to the waist of the atomic cloud.

E. Diffraction phase

If the initial atomic state has some velocity with respect to the lattice when being loaded into the lattice, the resulting state is a superposition of even-parity and odd-parity states, which can lead to a diffraction phase. For a plane-wave state with initial velocity $\pm \delta v$ in the first Brillouin zone, the resulting decomposition when loaded into the lattice will be the superposition $|\psi_i\rangle = \sqrt{(v_r - \delta v)/v_r} |+_gs\rangle \pm \sqrt{\delta v/v_r} |-_gs\rangle$ by momentum conservation. Figures 11 and 12 show numerical simulations of the diffraction phase for a $16\hbar k$ Bloch beamsplitter. Almost all of the diffraction phase from the beamsplitter comes from the first $8\hbar k$ momentum splitting near velocity degeneracy because the energies of the even- and odd-parity ground states differ here; further increasing the momentum transfer beyond this does not increase the diffraction phase. The diffraction phase for a beamsplitter scales like the square root of the initial velocity, which is related to the above decomposition into eigenstates, but the prefactor in front of this scaling can be controlled by varying the lattice depth and the details of loading or unloading the lattice. The simulations in Figures 11 and 12 use a linear intensity ramp for loading an unloading over a time $t_{\text{load}} = 6\pi\omega_r^{-1}$.

Figure 12 shows the diffraction phase as a function of the lattice depth, and oscillations in the diffraction phase allow one to operate at a “magic” lattice depth with suppressed sensitivity to diffraction phases from missing the center velocity of the atom cloud. For precision measurement, such magic lattice depths could be used to significantly reduce the diffraction phases caused by fluctuations in experimental parameters. For example, a ramp rate of $r = 4\omega_r^2$ and a lattice depth around $U_0 = 5.9E_r$ gives 80% efficient beamsplitters with minimized diffrac-

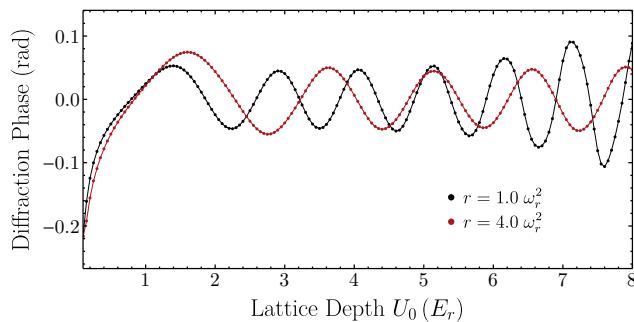


FIG. 12. Numerical simulation of diffraction phase from a Bloch beamsplitter as a function of lattice depth for two different ramp rates, using an initial velocity with respect to the lattice of $0.001v_r$. Points are from simulation, lines are an interpolation between points to guide the eye. The zero crossings in the diffraction phase allow for one to operate an interferometer at a “magic” lattice depth to suppress sensitivity to diffraction phase. See text for further discussion.

tion phase sensitivity (see Figures 5 and 12). We can reasonably operate within $0.001v_r$ of the center velocity of the atom cloud, and by intensity stabilizing the lattice to 1% fluctuations, the diffraction phase can be limited to ± 10 mRad. This diffraction phase can then be measured directly by varying the duration of the interferometer, as done in reference [1].

F. Symmetrized Hamiltonian

The Hamiltonian in Eq. (5) can be explicitly symmetrized by applying a rotation to the basis states. This is achieved by rotating to new basis states that are symmetric and antisymmetric combinations of the free-space momentum basis states, namely $|+l\rangle = |l\rangle + |-l\rangle$ and $|-l\rangle = |l\rangle - |-l\rangle$. The zero momentum state remains unchanged under this rotation. The following rotation matrix achieves this:

$$R = |0\rangle\langle 0| + \sum_{l>0} \frac{1}{\sqrt{2}} (|l\rangle\langle l| + |-l\rangle\langle -l|) + \frac{1}{\sqrt{2}} (|l\rangle\langle -l| - |-l\rangle\langle l|) \quad (16)$$

The Hamiltonian (5) can then be rotated to the symmetric Hamiltonian $H_{\text{sym}} = RH_{\text{DLBO}}R^T$ to arrive at the following:

$$H_{\text{sym}} = \frac{(Ft)^2}{2m} |0\rangle\langle 0| + \sum_{l>1} \left(\frac{(2|l|\hbar k - Ft)^2}{2m} (|+l\rangle\langle +l| + |-l\rangle\langle -l|) + \frac{U_0}{2} (|+l\rangle(\langle +l+1| + \langle +l-1|) + |-l\rangle(\langle -l+1| + \langle -l-1|)) \right) + \frac{U_0}{2} (|+1\rangle\langle +2| + |-1\rangle\langle -2|) + \frac{U_0}{\sqrt{2}} (|0\rangle\langle +1| + |+1\rangle\langle 0|) \quad (17)$$

In this rotated basis, there is no coupling between $|0\rangle$ and $|-1\rangle$, so we can explicitly see why the odd-parity states have no level crossing near velocity degeneracy. Moreover, the coupling between $|0\rangle$ and $|+1\rangle$ is $\sqrt{2}$ larger than any of the other couplings, resulting in less Landau-Zener tunneling from this first level-crossing.

G. Higher-order generalization of the dual-lattice methods

The transitions driven in DLBO are two-photon processes that transfer $2\hbar k$ momentum. By sweeping past multiple of these transitions in successions, LMT can be easily achieved. In contrast, higher-order transitions are also possible that transfer $2n\hbar k$ momentum in a single, multi-photon process.

It is instructive to first understand single-lattice higher-order processes before understanding the dual-lattice analogues. SLBO can be thought of as adiabatically sweeping past a successions of $2\hbar k$ Bragg transitions [29]. The higher-order, multi-photon analogue has been implemented experimentally in reference [45]. The laser is adiabatically swept across a $2n\hbar k$ Bragg resonance, which adiabatically drives a $2n$ -photon process. Though not discussed directly in [45], this process can be interpreted using a Bloch band picture where atoms have an initial quasimomentum outside of the first Brillouin zone such that they are loaded into higher Bloch bands. As the lattice is accelerated, the state sweeps past a level crossing between higher Bloch bands, and successful momentum transfer requires the state to adiabatically traverse the crossing and stay in the same Bloch band.

DLBO can be thought of as adiabatically sweeping past a succession of “double Bragg” transitions [46]. A first-order double Bragg transition symmetrically drives $\pm 2\hbar k$ Bragg resonances such that the two arms are split by $4\hbar k$ momentum. One can also symmetrically drive two higher-order Bragg resonances that transfer $\pm 2n\hbar k$ momentum to obtain a $4n\hbar k$ beamsplitter, as are implemented in references [13, 23].

It is also possible to adiabatically sweep past a higher-order double Bragg transition. In terms of the modulation frequency ω_m in Eq. (1), these resonances occur at $\omega_m = (2m+1)\omega_r$ for integers m . A $4n\hbar k$ adiabatic dual-lattice beamsplitter can be achieved by sweeping past

one of these resonances adiabatically. An experimental sequence would consist of the following: 1) atoms are adiabatically loaded into a lattice with a modulation frequency slightly below the desired resonance, 2) the modulation frequency is swept across the resonance, and 3) the atoms are adiabatically unloaded from the lattice. It is important that the modulation frequency does not become close to other resonances during this sequence. Unlike a Bloch beamsplitter, continued ramping of ω_m after a high-order beamsplitter process will not transfer more momentum, but rather alternate between increasing and decreasing the momentum splitting between arms. The average momentum transfer per Bloch period will still be $4\hbar k$, as in the ground band.

Our simulations of this process show that it can be more efficient than a Bloch beamsplitter at a given ramp rate. However, there are two major downsides to these higher-order dual-lattice techniques. First, much more laser power is required to drive the transition; the power required to drive an n^{th} -order Bragg transition scales sharply with the order n [15]. Second, continued ramping of the lattices does not continue to increase momentum splitting in any advantageous way compared to using the ground band. As a result, the first-order dual-lattice methods discussed in the main text are easier to use if the goal is to achieve very large momentum splitting without the need for significantly more laser power.

-
- [1] R. H. Parker, C. Yu, W. Zhong, B. Estey, and H. Müller, *Measurement of the fine-structure constant as a test of the Standard Model*. Science 360, 191-195 (2018)
- [2] R. Bouchendira, P. Clad, S. Guellati-Khélifa, F. Nez, and F. Biraben, *New Determination of the Fine Structure Constant and Test of the Quantum Electrodynamics*. Phys. Rev. Lett. 106, 080801 (2011)
- [3] G. Rosi, F. Sorrentino, L. Cacciapuoti, M. Prevedelli & G. M. Tino, *Precision measurement of the Newtonian gravitational constant using cold atoms*. Nature 510, 518521 (2014)
- [4] J. B. Fixler, G. T. Foster, J. M. McGuirk, M. A. Kasevich, *Atom Interferometer Measurement of the Newtonian Constant of Gravity*. Science 315, 5808 74-77 (2007)
- [5] L. Zhou, S. Long, B. Tang, X. Chen, F. Gao, W. Peng, W. Duan, J. Zhong, Z. Xiong, J. Wang, Y. Zhang, and M. Zhan, *Test of Equivalence Principle at 10^{-8} Level by a Dual-Species Double-Diffraction Raman Atom Interferometer*. Phys. Rev. Lett. 115, 013004 (2015)
- [6] G. Rosi, G. D'Amico, L. Cacciapuoti, F. Sorrentino, M. Prevedelli, M. Zych, Č. Brukner, and G. M. Tino, *Quantum test of the equivalence principle for atoms in coherent superposition of internal energy states*. Nature Communications volume 8, Article number: 15529 (2017)
- [7] P. Hamilton, M. Jaffe, P. Haslinger, Q. Simmons, H. Müller, and J. Khoury, *Atom-interferometry constraints on dark energy*. Science, 349, 849 (2015)
- [8] M. Jaffe, P. Haslinger, V. Xu, P. Hamilton, A. Upadhye, B. Elder, J. Khoury, and H. Müller, *Testing sub-gravitational forces on atoms from a miniature in-vacuum source mass*. Nature Physics 13, 938942 (2017)
- [9] L. Zhou, Z. Y. Xiong, W. Yang, B. Tang, W. C. Peng, K. Hao, R. B. Li, M. Liu, J. Wang, and M. S. Zhan, *Development of an atom gravimeter and status of the 10-meter atom interferometer for precision gravity measurement*. Gen. Relativ. Gravit. 43, 19311942 (2011)
- [10] X. Wu, Z. Pagel, B. S. Malek, T. H. Nguyen, F. Zi, D. S. Scheirer, and H. Müller, *Gravity surveys using a mobile atom interferometer*. arXiv:1904.09084 [physics.atom-ph]
- [11] P. Asenbaum, C. Overstreet, T. Kovachy, D. D. Brown, J. M. Hogan, and M. A. Kasevich, *Phase Shift in an Atom Interferometer due to Spacetime Curvature across its Wave Function*. Phys. Rev. Lett. 118, 183602 (2017)
- [12] S. Chiow, T. Kovachy, H. Chien, and M.A. Kasevich, *102hk Large Area Atom Interferometers*. Phys. Rev. Lett. 107, 130403 (2011)
- [13] M. Gebbe, S. Abend, J.N. Siemß, M. Gersemann, H. Ahlers, H. Müntinga, S. Herrmann, N. Gaaloul, C. Schubert, K. Hammerer, C. Lämmerzahl, W. Ertmer, and E. M. Rasel, *Twin-lattice interferometry*. In preparation.
- [14] H. Müller, S. Chiow, Q. Long, S. Herrmann, and S. Chu, *Atom Interferometry with up to 24-Photon-Momentum-Transfer Beam Splitters*. Phys. Rev. Lett. 100, 180405 (2008)
- [15] H. Müller, S. Chiow, and S. Chu, *Atom-wave diffraction between the Raman-Nath and the Bragg regime: Effective Rabi frequency, losses, and phase shifts*. Phys. Rev. A 77, 023609 (2008)
- [16] B. Estey, C. Yu, H. Müller, P.-C. Kuan, and S.-Y. Lan, *High sensitivity, low-systematics atom interferometers using Bragg diffraction and Bloch oscillations*. Physical Review Letters 115, 083002 (2015)
- [17] R. H. Parker, C. Yu, B. Estey, W. Zhong, E. Huang, and H. Müller, *Controlling the multiport nature of Bragg diffraction in atom interferometry*. Phys. Rev. A 94, 053618 (2016)
- [18] A. O. Jamison, B. Plotkin-Swing, and S. Gupta, *Advances in precision contrast interferometry with Yb Bose-Einstein condensates*. Phys. Rev. A 90, 063606 (2014)
- [19] M.B. Dahan, E. Peik, J. Reichel, Y. Castin, and C. Salomon, *Bloch Oscillations of Atoms in an Optical Potential*. Phys. Rev. Lett. 76, 4508 (1996)
- [20] M. Cadoret, E. de Mirandes, P. Cladé, S. Guellati-Khélifa, C. Schwob, F. Nez, L. Julien, and F. Biraben, *Combination of Bloch Oscillations with a Ramsey-Bord Interferometer: New Determination of the Fine Structure Constant*. Phys. Rev. Lett. 101, 230801 (2008)
- [21] V. S. M. and P. R. Berman, *Momentum transfer using chirped standing-wave fields: Bragg scattering*. Physical Review A 68, 023610 (2003)
- [22] H. Müller, S. Chiow, S. Herrmann, and S. Chu, *Atom interferometers with scalable enclosed area*. Physical Review Letters 102, 240403 (2009)
- [23] S. Abend, *Atom-chip gravimeter with Bose-Einstein condensates*. Ph.D. dissertation, Leibniz University Hannover (2017)
- [24] P. W. Graham, J. M. Hogan, M. A. Kasevich, and S. Rajendran, *A Resonant Mode for Gravitational Wave De-*

- tectors based on Atom Interferometry*. Phys. Rev. D 94, 104022 (2016)
- [25] D. Gao, J. Wang, and M. Zhan, *Atomic Interferometric Gravitational-wave Space Observatory (AIGSO)*. Commun. Theor. Phys. 69, 37 (2018)
- [26] C. Yu W. Zhong B. Estey J. Kwan R. H. Parker, H. Müller, *Atom Interferometry Measurement of the Fine Structure Constant*. Annalen Der Physik 531, 5 (2019).
- [27] Pierre Cladé, *Bloch oscillations in atom interferometry*. International School of Physics Enrico Fermi (2014) jhal-00989685
- [28] A. R. Kolovsky and H. J. Korsch, *Bloch oscillations of cold atoms in optical lattices*. International Journal of Modern Physics B, 18, 9, pp. 1235-1260 (2004)
- [29] E. Peik, M. B. Dahan, I. Bouchoule, Y. Castin, and C. Salomon, *Bloch oscillations of atoms, adiabatic rapid passage, and monokinetic atomic beams*. Physical Review A, 55, 2989 (1997)
- [30] T. Kovachy, J. M. Hogan, D. M. S. Johnson, and M. A. Kasevich, *Optical Lattices as Waveguides and Beam Splitters for Atom Interferometry: An Analytical Treatment and Proposal of Applications*. Physical Review A 82, 013638 (2010)
- [31] Q. Niu and M.G. Raizen, *How Landau-Zener Tunneling Takes Time*. Physical Review Letters, 80, 16 (1998)
- [32] L.T.A. Ho & L. F. Chibotaru, *A simple derivation of the Landau-Zener Formula*. Physical Chemistry Chemical Physics 16(15) (2014)
- [33] S. Abend, M. Gebbe, M. Gersemann, H. Ahlers, H. Müntinga, E. Giese, N. Gaaloul, C. Schubert, C. Lämmerzahl, W. Ertmer, W. P. Schleich, & E. M. Rasel, *Atom-Chip Fountain Gravimeter*. Phys. Rev. Lett. 117, 203003 (2016)
- [34] C. Wachter, *Numerical Solution of the Time-Dependent 1D-Schrödinger Equation using Absorbing Boundary Conditions*. Bachelor's Thesis, University of Graz (2017)
- [35] M. Büchner, R. Delhuille, A. Miffre, C. Robilliard, J. Vigué and C. Champenois, *Diffraction phases in atom interferometers*. Phys. Rev. A 68, 013607 (2003)
- [36] B. Estey, C. Yu, P.C. Kuan, S.Y. Lan, and H. Müller, *High-Resolution Atom Interferometers with Suppressed Diffraction Phases*. Phys. Rev. Lett. 115, 083002 (2015)
- [37] B. Estey, *Precision Measurement in Atom Interferometry Using Bragg Diffraction*. Ph.D. dissertation, University of California, Berkeley (2016)
- [38] D. M. Stamper-Kurn, G. E. Marti, and H. Müller, *Verifying quantum superpositions at metre scales*. Nature 537, p. E1E2 (2016)
- [39] E. R. Elliott, M. C. Krutzik, J. R. Williams, R. J. Thompson, and D. C. Aveline, *NASAs Cold Atom Lab (CAL): system development and ground test status*. NPJ Microgravity, 4, 16 (2018)
- [40] S. Kulas, C. Vogt, A. Resch, J. Hartwig, S. Ganske, J. Matthias, D. Schlippert, T. Wendrich, W. Ertmer, E. M. Rasel, M. Damjanic, P. Weßels, A. Kohfeldt, E. Luvsandamdin, M. Schiemangk, C. Grzeschik, M. Krutzik, A. Wicht, A. Peters, S. Herrmann, C. Lämmerzahl, *Miniaturized lab system for future cold atom experiments in microgravity*. Microgravity Sci. Technol. 29: 37 (2017)
- [41] F. Bloch, *Über die Quantenmechanik der Elektronen in Kristallgittern*. Z. Physik 52: 555 (1929)
- [42] W.L. Bragg, *The Diffraction of Short Electromagnetic Waves by a Crystal*. Proceedings of the Cambridge Philosophical Society, 17, 43-57 (1913)
- [43] P. Cladé, T. Plisson, S. Guellati-Khélifa, F. Nez, F. Biraben, *Theoretical Analysis of a Large Momentum Beamsplitter using Bloch Oscillations*. hal-00503824f (2010)
- [44] C. Yu, *Measuring the fine structure constant with a state-of-the-art atom interferometer*. Ph.D. dissertation, University of California, Berkeley (2018)
- [45] T. Kovachy, S. Chiow, and Mark A. Kasevich, *Adiabatic-rapid-passage multiphoton Bragg atom optics*. Physical Review A 86, 011606, 2012
- [46] E. Giese, A. Roura, G. Tackmann, E. M. Rasel, and W. P. Schleich, *Double Bragg diffraction: A tool for atom optics*. Phys. Rev. A 88, 053608 (2013)